Delft University of Technology

A high resolution interferometric method to measure local swelling due to CO₂ exposure in coal and shale

Pluymakers, A.; Liu, J.; Kohler, F.; Renard, F.; Dysthe, DK

Important note
To cite this publication, please use the final published version (if applicable).
Please check the document version above.

A high resolution interferometric method to measure local swelling due to CO$_2$ exposure in coal and shale

Pluymakers A.[b,*], Liu J.[c,d], Kohler F.[a], Renard F.[a,e], Dysthe D.[a]

[a] *PGP, University of Oslo, Postboks 1048, 0316 Oslo, Norway*
[b] *Department of Geoscience and Engineering, Delft University of Technology, 2128 CN Delft, Netherlands*
[c] *Department of Mechanical Engineering, Eindhoven University of Technology, 5600 MB Eindhoven, Netherlands*
[d] *Department of Earth Sciences, Utrecht University, 3584 CD Utrecht, Netherlands*
[e] *University Grenoble Alpes & CNRS, ISTerre, Grenoble, France*

ABSTRACT

We present an experimental method to study time-dependent, CO$_2$-induced, local topography changes in mm-sized composite samples, plus results showing heterogeneous swelling of coal and shale on the nano- to micrometer scale. These results were obtained using high resolution interferometry measurements of sample topography, combined with a new type of experimental microfluidic device. This device is a custom-built pressure vessel, which can contain any impermeable sample type and can be placed under any microscope. The pressure vessel itself has been tested to handle pressures up to 100 bar at room temperature conditions. For the experiments reported here we used three sample types: i) epoxy and dolomite, ii) coal, epoxy and dolomite and iii) shale. These model systems (thicknesses between 2 and 10 mm) were exposed to pressurized CO$_2$ (20–35 bars) and subsequently deformation over time was monitored with a white light interferometer. This provided a lateral spatial resolution of 979 nm and a vertical spatial resolution of 200 nm, i.e. sufficient resolution so that coal and shale constituents can be tracked individually. Within 72 h epoxy swells homogeneously up to 11 μm, coal swells 4 ± 1 μm and dolomite is unreactive with the dry CO$_2$ injected here, and as such is used as a reference surface. The differential swelling of coal can be correlated in space with the macerals, where macerals with an initial higher topography swell more. The average or bulk swelling exhibits an approximate t$^{1/2}$ relation, indicative of diffusion-controlled adsorption of CO$_2$ on the organic matter. Measurements of the differential swelling of both shale samples enabled tracking of individual patches of organic matter within the shale (max. 20 × 20 μm). These patches exhibit finite swelling of on average 250 nm in 4 h (in the Pomeranian shale) and 850 μm in 20 h (in the Green River shale), where total swelling is assumed to be related to the volume of the patches of organic matter.

1. Introduction

Gases such as CO$_2$ and CH$_4$ lead to swelling of coal (e.g. Day et al., 2008; Hol and Spiers, 2012; Karacan, 2007, 2003; Liu et al., 2015) and shale and clay (e.g. Busch et al., 2016, 2008; de Jong et al., 2014). The heterogeneous deformation of these materials can have opposite effects. It may either inhibit the reactive transport as swelling clogs transport pathways, or enhance reactive transport in those cases where shrinkage creates new transport pathways or when heterogeneous swelling leads to microfracturing. To date, experimental work investigating the permeability and permeability change of a porous medium relied on batch reaction or flow-through set-ups (see Rohmer et al., 2016 for a review of different experimental techniques). Reaction experiments are usually performed in closed pressure vessels, with observation before and after the experiment, i.e. static measurements (for example, Liu et al., 2012). Traditional flow-through experiments capture some of the dynamics of reactive transport, usually by monitoring pressure and chemistry at the in- and the outlet (for example, Bachaud et al., 2011; Edlmann et al., 2013; Elkhoury et al., 2013; Ellis et al., 2011; Olabode and Radonjic, 2014). However, this type of measurements does not provide information where liquid goes, nor on how it interacts with the solid. Over the years different instruments have been used to monitor in-situ fluid-rock interaction using pressurized fluids, such as an eddy current sensor (Hol and Spiers, 2012), in-situ X-ray diffraction (Giesting et al., 2012), regular digital cameras (Day et al., 2008; Perrier et al., 2017), optical microscopy (van Bergen et al., 2009), secondary electron

---

microscopy (Wang et al., 2017), X-ray micro-tomography (Karacan, 2007, 2003; Kobchenko et al., 2011; Nguyen et al., 2013) and micro-fluidic devices (Neuville et al., 2016; Porter et al., 2015). All of these experimental methods have their own advantages and disadvantages in terms of sample size, resolution, and pressure/temperature/fluid conditions that can be obtained.

To image and quantify surface topography changes with sub-micrometer resolution, we developed a new versatile micro-sized pressure chamber that is suitable for placement under a microscope. The design of our device is such that any type of low permeability reactive material can be inserted and different types of reactive liquids or gases can be used. Moreover, the optical accessibility of the sample allows for observation using various microscopy techniques, including white light interferometry. The latter technique is presented here and it provides nanometer resolution topography measurements of rough surfaces (up to tens of micrometers) by comparing the wavelength, and hence travel path, of a split light beam. Additionally, we developed the accompanying data processing routine necessary to register and correct an image time series, which is affected by small lateral drifts of the system. The data processing technique also takes the pixels with incomplete height reconstruction into account. These in-situ white light interferometer measurements allow tracking of the differential surface deformation of various materials in time and space.

This new method can be a useful tool for future studies of local reactions that induce surface changes in solid materials under high pressures. It may have impact on diverse industry-related problems, such as corrosion, mineral reactions and coal mining with economic and social implications, especially combined with complementary techniques such as sorption experiments (e.g. Lutyński et al., 2017) or small angle neutron or X-ray scattering (SANS/SAXS) measurements (e.g. Radlinski et al., 2004). Specifically, industry practices such as CO_2 sequestration and/or enhanced hydrocarbon recovery inject high pressure CO_2, captured at power plants, into the subsurface for geological storage and/or enhanced hydrocarbon recovery. Aimed at improving our understanding of reactivity and dynamic flow properties as a result of CO_2-induced swelling in coal and shale gas reservoirs, we report here the results of three types of experiments on materials that react with gaseous CO_2 at room temperature conditions: i) samples with epoxy and dolomite, ii) samples with coal, epoxy and dolomite and iii) samples with shale. These samples were exposed to pressurized CO_2 (20–35 bars) and subsequently deformation over time was monitored using white light interferometry.

In enhanced coal bed methane, CO_2 is used to enhance methane production (e.g. Moore, 2012). In this technique, the coal bed permeability (as determined by the permeability of cleats plus that of the bulk material) is the most important factor determining the ease and efficiency of recovery. Bulk measurements of sorption of methane (e.g. Liu et al., 2017) and ethane (Staib et al., 2014) versus bulk measurements of CO_2 adsorption (e.g. Hol and Spiers, 2012) show that if these processes occur in sequence, the competitive sorption will likely lead to shrinkage followed by swelling (already proposed by Brochard et al., 2012). The difference in acquired strain will determine the eventual permeability. Lin et al. (2017) showed that the bulk strain resulting from sorption in a cm-sized core sample is for CO_2 twice that for CH_4. Moreover, bulk measurements have shown that the final swelling rate of different coal types are correlated to maceral content, where vitrinite-rich coals exhibit slower bulk swelling rates (Staib et al., 2014). Furthermore, exposure to CO_2 has been shown to lead to micro-fracturing, postulated to be related to the differential swelling of different macerals (Hol et al., 2012). Therefore, a method that can successfully capture the dynamic behavior of local macerals plays an important role in better quantifying permeability evolution during enhanced coal bed methane recovery in coal seams. Measuring swelling through visualization of a coal surface captures such local deformation. However, the existing methods have disadvantages, such as low spatial and vertical resolution (10 μm lateral resolution; Day et al., 2008), or

the lack of a possibility to image the exact same surface with other microstructural techniques (250 μm voxelsize; Karacan, 2007, 2003). Our technique has an unprecedented submicrometer lateral resolution and vertical nanometer resolution, and the same surface can be imaged as well with other optical microscopy techniques, and electron microscopy.

Shale is a strongly heterogeneous rock, with different components that can interact with CO_2 with opposite results in terms of permeability. Individual clay minerals are capable of incorporating CO_2 and thus exhibit CO_2-induced swelling (Busch et al., 2016; de Jong et al., 2014), but it has also been hypothesized that shrinkage occurs if CO_2 leads to dehydration of the mineral structure. Both dehydration and swelling may lead to intercrystalline stresses and hence microfractures (Busch et al., 2016; Ougier-Simonin et al., 2016). Moreover, shales often contain organic matter. Given that coal, i.e. organic matter, exhibits strong swelling upon CO_2 exposure (Hol and Spiers, 2012), CO_2 sorption to organic matter in shale may lead to local swelling as well (cf. Busch et al., 2016). Because of the preferential sorption of CO_2 to organic matter over methane, it has also been to proposed to use CO_2 for enhanced gas recovery in shale gas plays (Middleton et al., 2015). The competition between swelling, fracturing and permanent CO_2 storage determines the final suitability of a CO_2 storage site versus the use of CO_2 as a fracturing fluid. Note that the heterogeneous swelling behavior of shale has been demonstrated using electron microscopy and exposure to different humidity levels (Wang et al., 2017), but high resolution measurements using CO_2 are lacking.

2. Materials and method

We measure how sample topography changes over time using a white light interferometer with a new micro-pressure chamber designed and built at the University of Oslo. The preparation of the sample, device assembly, procedure and determination of the vertical resolution of the time series are described below.

2.1. Sample preparation

The sample of choice is embedded into a 2-component Epofix epoxy. Using epoxy enables attaching high pressure tubing to any type of sample. To construct the samples, we first prepare a cylindrical epoxy base of 25 mm diameter and 5–10 mm height that contains the mm-sized rock sample. Since the window size has a 5 mm diameter, if rock samples are smaller than 5 × 5 mm, there will be some reactive epoxy in the CO_2-exposed area. For such rock + epoxy samples, repeated use with CO_2 may lead to rock fracture due to epoxy swelling. After curing, the epoxy base with rock sample is polished until mirror-smooth, going step-wise up to 4000 grit silicon carbide sandpaper, and finished with a polishing cloth and diamond suspension (1 μm particles). Subsequently we drill the holes for the tubing into the epoxy assembly in two phases: a small diameter (0.6 mm) hole on the sample side, and a larger hole on the other side (1.5 mm; see Fig. 1c; Fig. 1d). Before further construction, this base can be imaged with regular optical microscopy and/or electron microscopy (with or without element determination with Energy-Dispersive X-ray Spectroscopy) if needed. After imaging, a high pressure steel tube is roughened with 40 grit sandpaper, and glued in the 1.5 mm hole using brush-on Loctite superglue. The pressure tubing is then fixed with a second epoxy layer, giving a total sample height of 15–25 mm. An example sample containing dolomite and coal in epoxy is shown in Fig. 1c.

2.2. Pressure vessel construction

The sample is inserted in the brass pressure vessel (Fig. 1a; Fig. 1d), with a stainless steel lid with six stainless steel sunken screws and a center hole with 60° edges for microscope access. Below the sample is a soft, donut-shaped, silicone rubber plug (custom-made using Ecoflex
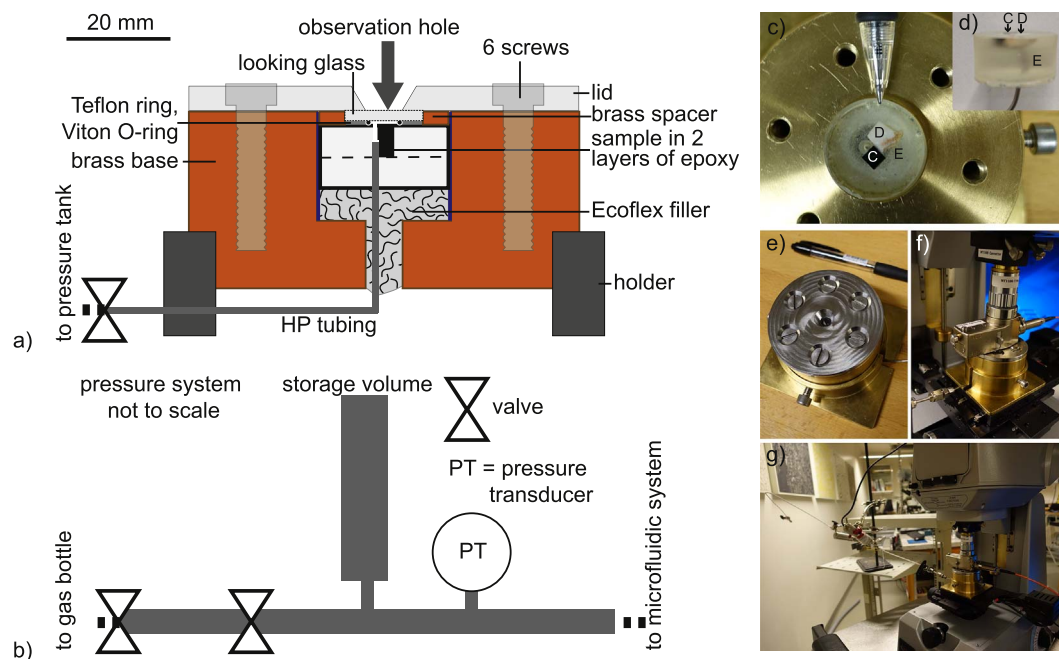
Fig. 1. a) microfluidic sample assembly; b) pressure system, not to scale; c) top view of dolomite (D)/epoxy (E)/coal (C) sample (used for dolcoal1, 2 and 3), pen for scale; d) side view of c); e) assembled pressure device; f) assembly underneath the white light interferometer; g) assembly plus pressure vessel under the white light interferometer.

00-20, manufactured by Smooth-on), to ensure the sample straightens as the lid is screwed on. On top of the sample rests a 2.45 mm thick donut-shaped brass spacer, encircling a 0.7 mm high Teflon back-up ring and a 5 × 1 mm Viton O-ring. The glass lid is microscope-quality uncoated H-K9L glass, with a diameter of 15 mm, and a thickness of 1.75 mm. It fits the brass spacer and rests on top of the O-ring which is supported by the Teflon back-up ring. The Teflon back-up ring ensures there will be a micro-pressure chamber between the sample surface and the glass once the O-ring is activated, which is approximately 700 μm high and 5 mm in diameter. Nitrile sleeves ensure that the spacer/glass/O-ring assembly remains centered on the sample.

The pressure tubing is connected to a pressure system (Fig. 1b; Fig. 1f), constructed out of 1/8′ tubing, a cm-sized pressure chamber and a WIKA PT-30 pressure transducer. The entire assembly is pressure-tested up to 100 bar using N_2 gas. Since the pressure system is much bigger than the micro-pressure chamber, pressure equilibration between the micro-pressure chamber and the pressure vessel will lead to a stable pressure close to the initial pressure of the pressure vessel. These experiments can thus be performed without a pump. At the used pressures the pressure drop when opening the tap between micro-pressure chamber and pressure vessel is at maximum 1 bar. A potential and simple upgrade of the assembly would be the addition of a pump to ensure a more stable pressure, avoiding the small pressure differences present in our experiments, which were due to minor leakages and room temperature changes.

2.3. Experimental procedure

Sample topography (i.e. pixel height *z* as a function of position *x, y*) was measured directly through a glass window by use of a white light interferometer (Wyko NT1100; Fig. 1f; Fig. 1g)) equipped with a Through Transmissive Media module (Fig. 1e) plus Veeco software. The interferometer is placed on a damped table. Vertical nanometer resolution is achieved for single measurements. In the cases presented here, scanning was performed in vertical scanning mode, using a 20 × Veeco objective and a field of view lens of 0.5. The manufacturer specifies that this configuration allows for sampling distances (i.e. pixel size in the height images) of 979 nm, where maximum field of view is

626 × 426 μm. Total scan length in vertical scanning mode was up to 50 μm. The minimum time-lapse measurement interval for this Wyko NT1100 interferometer is ~3 min. In the experiments presented here the exact time intervals varied from experiment to experiment. They typically ranged from 3 to 5 min in the first hour of the experiment, to 10, 15 or 30 min during the remainder of the experiment. Pressure was logged using the native pressure transducer WIKA software with a 30 or 60 s interval.

Each experiment is preceded by calibration of the vertical scanning imaging mode of the interferometer using a mirror with a 10 μm height step. The pressure reservoir is filled with bottle pressure CO_2 gas, and the desired pressure is obtained by stepwise escape of CO_2. The brass base plus sample are fixed to the white light interferometer stage. A reference glass (10 mm diameter, 1.75 mm thickness) is placed in the Through Transmissive Media module, and a duplicate zero measurement is taken whilst the sample is at ambient conditions. The experiment starts by opening the tap between sample and reservoir, pressurizing the micro-pressure chamber between sample and glass.

Following adjustment of focus and stage tilt to achieve optimal imaging conditions, the time-lapse imaging sequence is set. Due to drift during long duration experiments (12 + hours), occasionally tilt and/or focus need to be slightly readjusted. Experiments are halted by stopping time-lapse imaging and recording a dual measurement, before pressure is released and pressure logging halted. If desired, it is possible to also record the desorption process and associated shrinkage of the sample.

2.4. Data processing

The raw topography data obtained from the white light interferometer is affected by missing height information, outliers and vertical and horizontal drift of the sample. To determine spatially resolved swelling and shrinkage behavior of the material we developed a data processing procedure, written in Matlab and schematically represented in Fig. 2. The results of the intermediate steps are shown in Supplementary Video V1 for experiment dolcoal3. Some of the materials observed in this experiment have micrometer topography on the observed interface, such as fractures or pores, as well as a small percentage of dispersed grains with relatively high reflectance. Moreover, the white

light interferometer is limited to a certain range of height variations and reflectance for one focal position and one acquisition moment of the camera at the time. Together, this means that the resulting data sets contains pixels at which the height information could not be obtained. As a first step, we dismissed the datasets with > 15% pixels without height data. The image registration is done in an interactive semi-automated way. First, the datasets are brought to the same plane using the average of a reference area, which is either an inert area (dolomite in our test cases), or the full sample window, i.e. for single material samples (used for the shale samples). In the former case, zero swelling means no reaction at all, i.e. since dolomite is inert to dry CO_2 exposure. However, in the latter case, only local variations in relative swelling or shrinkage can be distinguished, so no uniform trend of the entire sample area coming up or down can be measured. In this case, zero swelling means just as much reaction as the average surface area. Moreover, if the surface overall swells, the areas that swell less than the average will appear to shrink instead. Apparent shrinkage in such experiments can thus also mean less swelling than the average. After all data is on the same plane, outliers of > 3 × the standard deviation of the comparison of the topography with the median-filtered topography are removed. After removal of tilts using fits to an averaged cross section in x and y directions, a fine tuning of the vertical axis is performed using the same reference area as used to bring all measurements to the same plane. Subsequently, an estimate of the missing and removed pixel values is gained by interpolation. The lateral data registration is done by cross correlation with a reference dataset taken, e.g., at the beginning of the measurement. Note that with the chosen cross correlation function, cross correlation would be impossible if there was significant lateral motion of the samples throughout the experiment. Finally, time-resolved variations in the surface topography are obtained by subtraction of datasets at successive time steps. Given the fine grain size of clays, for heterogeneous shale plotting the standard deviation of each pixel through time allows determining areas with large relative movement as the areas of interest. Subsequent use of a low-pass filter (with a filter kernel similar to either the grain size of the larger clasts or of individual clay clusters) helps reducing noise and helps to distinguish trends.

2.4.1. Vertical resolution of a time-series

Single measurements with this white light interferometer can reach nanometer height resolution. However, given this nanometer resolution, the measurement of multiple datasets over time means that small changes in the mechanical parts actually can lead to small drifts, for
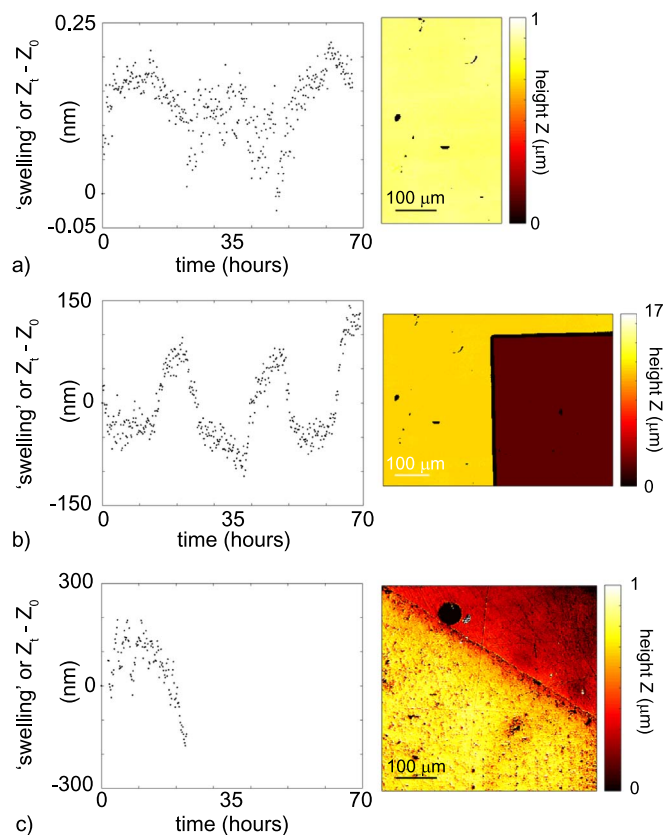

Fig. 3. White light interferometer reference measurements of three different surfaces under ambient conditions. 'Swelling' versus time on the right and a map view of the starting topography on the left. 'Swelling' is in this case the average topography of the total sample at time t (Z_t) minus the average topography at the starting time (Z_0) versus time, where an increase in height is defined positive (hence swelling); a) a smooth reference mirror (no steps); b) including one 10 μm step and c) of a dolomite/epoxy interface. The oscillations in b) are related to day-night variations in room temperature.

example caused by variations in temperature and air currents in the room. The changes in room temperature also cause small pressure changes in the CO_2 reservoir, leading to additional movement due to the compressibility of the system. Apart from these reasons for physical drift, there is also apparent drift due to the presence of unexposed areas. To determine the combined effect of these factors, we performed a 24 h

---

Selection of useful datasets:
- Filtering out incomplete datasets
  (more than 15% pixels without height information)

Correction of drifts of the measurement system by 3D dataset registration:
- Adjustment of average height (coarse, using reference area if available) – see image 2 in Video S1
- Removing of outliers – see image 3 in Video S1
- Tilt adjustment – see image 4 in Video S1
- Adjustment of height (fine, using reference area if available)
- Interpolation of missing and removed (outliers) pixels – see image 5 in Video S1
- Lateral registration by cross correlation – see image 6 in Video S1

Detection of local surface variations (deformation, swelling)
- Difference to reference data
- Removing of noise by spatial filtering considering the feature / grain
  size of the sample

Fig. 2. Schematic representation of the different steps of the data processing procedure. See Supplementary Video V1 for an example (dolcoal 3; the processed data are shown in Fig. 6) how the data evolves with each processing step.

measurement of an inert reference mirror with a 10 μm height step at ambient conditions with time-lapse imaging, as well as imaging over a dolomite/epoxy interface at ambient conditions. The part of the mirror surface without steps is measured within nanometer resolution also over time (Fig. 3a). Note that without topography, there is no possibility to account for any lateral drift, since this will simply not be registered. Both the averages of the entire mirror (including the 10 μm step) and the dolomite/epoxy interface show a variation of ± 100 nm over 24 h (Fig. 3b and c), due to lateral drift and the noise associated with topography. This means that the measurement and data-processing procedures as presented here can pick up lateral differences in swelling that exceed 200 nm. More stable systems and sophisticated analysis methods (for example, cross-correlation which would allow for subpixel shifts) can further increase the vertical resolution of this approach. The relatively large field of view (626 × 426 μm) combined with the high vertical resolution provides a huge advantage in comparison to the current techniques which can measure dynamic surface processes. It combines the vertical resolution of SEM measurements of local swelling in mudrocks (Wang et al., 2017) and the large lateral extent of measurements of camera observations of coal swelling (Day et al., 2008).

2.5. Sample-specific methods

The experiments presented here are listed in Table 1. We used dolomite without visible porosity as an inert material for epoxy-swelling tests, i.e. the dolomite was completely surrounded by epoxy. Given that epoxy exhibits strong swelling upon CO_2 exposure and that the geometry of these experiments was simple, they enabled us to develop the data processing routines, plus quantification of the swelling of epoxy. In the other demonstrations tests we used coal and shale as reactive geological materials. The following sample combinations were tested:

i). Dolomite/epoxy: not-swelling/large swelling. The dolomite is a pure natural dolomite, obtained from the undeformed wall rock from the Foiana fault zone, Italy. See Fondriest et al. (2015) for a description.

ii). Dolomite/coal/epoxy: not-swelling/intermediate, differential swelling/large swelling. The coal sample used in this study was collected from the Brzeszcze mine 364, Poland. It has a vitrinite reflectance of 0.77 ± 0.05%, and is composed of vitrinite (60.1%), liptinite (9.8%) and inertinite (30.1%); ash content is 5.2% (more details in Hol et al., 2011). The coal sample was cut (details in Liu et al., 2016) and subsequently inserted such that the images were taken of the bedding plane; any swelling would hence be perpendicular to bedding.

iii). Shale only: heterogeneous behavior. We used two fine-grained, dark gray shale types, both clay-rich and with < 10% organic matter:

o Pomeranian shale, fragile core-material (4 km depth) from Poland;

see Pluymakers et al. (2017) for a description. This is clay-rich material (50–70% clay + mica, no swelling clays), with up to 10% organic matter. Since this is dehydrated core material, in-situ porosity is impossible to estimate. The images are taken of the bedding plane; any swelling would hence be perpendicular to bedding.

o Green River shale, strong outcrop material from Utah, see Kobchenko et al. (2011) for a description. In terms of composition this is roughly similar to the Pomeranian shale. Porosity is 5% or less. The images are taken perpendicular to the bedding plane.

In the experiments presented here, we used CO_2 gas at maximum 35 bar, since for higher pressures the refractive index changes substantially with pressure (Michels and Hamers, 1937). This means that to perform experiments at CO_2 pressures above 35 bar the use of a pump in the assembly is strongly recommended. Note that the procedure described here would work using any medium (gas or liquid). Due to the non-reversible nature of the epoxy swelling tests we used new samples in both tests focusing on epoxy (dol2 and dol5). Since coal swelling upon CO_2 adsorption is nearly reversible after first exposure (Day et al., 2008; Hol et al., 2012), the coal swelling tests are performed with the same sample (in which the coal is 3.6 mm thick), even though the epoxy is permanently deformed after the first run. After each coal swelling experiment this sample is left in a vacuum chamber overnight. Otherwise, in between runs the samples are kept at ambient conditions. To minimize the leakage risk, all sample assemblies are pre-pressure tested with N_2 gas and subsequently the pressure is dropped down for 10–15 min using a Busch Zebra vacuum pump (model RH 0006 - 0030 A; pressure of 2.0×10^{-6} bar).

3. Results on local swelling

3.1. Swelling of epoxy with a dolomite reference: reference experiments

To test how measurable swelling is for a simple geometry and to develop the data-processing protocols, we performed epoxy swelling tests with dolomite as an inert sample (and thus providing a reference surface). Before CO_2 exposure, the difference in height between dolomite and epoxy is 3 to 3.5 μm (Fig. 4). Exposure to CO_2 leads to time-dependent non-uniform swelling of the epoxy (Supplementary Video V2 on dol2). There is less swelling near the boundary between dolomite and epoxy because of a no slip boundary condition at this location. At the end of the experiment the discrete step between the dolomite and epoxy is gradual over 400–500 μm (Fig. 4). For dol2 the maximum average epoxy swelling is ~9 μm, and for dol5 this is ~6 μ (Fig. 5). The best fit to the average swelling curve is swelling $\propto t^{0.63}$ for dol2 and swelling $\propto t^{0.42}$ for dol5, where t is the time from CO_2 gas injection.

The time power law exponent close to 0.5 suggests the rate is controlled by Fickian diffusion of CO_2 into epoxy. For dol5 we performed measurements up to 24 h after dropping the CO_2 pressure to atmospheric (not shown), which only showed about 2 μm recovery of the

Table 1
Experimental conditions. All experiments are performed in a room with a controlled temperature of 20 ± 1 °C.

Experiment name	Sample	Sample type	Pressure1 (bars)	Duration (hours)	Pressure2 (bars)	Duration (hours)
Epoxy swelling						
dol2	Dol2	dolomite/epoxy	34 ± 1	41		
dol5[a]	Dol5	dolomite/epoxy	28 ± 2	1	25 ± 1.2	17 h
Coal swelling						
DOLCOAL1[a]	Dolcoal1	Dolomite/epoxy/coalcube	27 ± 1	2	20 ± 1	15
DOLCOAL2			25.3 ± 1.2	22		
DOLCOAL3			33.3 ± 1	66		
Shale swelling						
CO_2_11	POM_12	Pomerianian shale	31 ± 1	41		
CO_2_12	GRS_2	Green River Shale	32 ± 1	44		

[a] These experiments experienced a pressure drop within a few hours after the experiment started. The pressure steps and their duration are indicated.
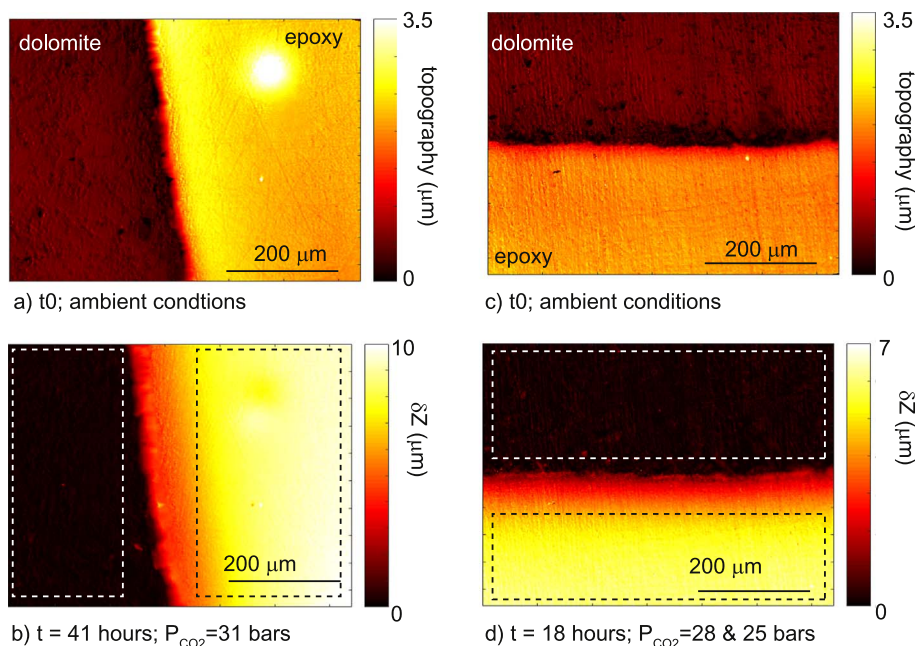
a) t0; ambient condtions

c) t0; ambient conditions

b) t = 41 hours; P_{CO_2}=31 bars

d) t = 18 hours; P_{CO_2}=28 & 25 bars

Fig. 4. Epoxy swelling. See also Supplementary Video V2, which shows how the surface dol2 swells through time; i.e. the equivalent of Fig. 4b. a) initial map of dolomite and epoxy for sample dol2; b) final differential map of dol2 showing δz (swelling, i.e. the change in surface topography), after ~40 h of exposure; c) initial map of dolomite and epoxy for sample dol5; d) final differential map of dol5 showing δz (swelling), after ~16 h of exposure. Squares indicate areas from which averages are taken that are shown in Fig. 5.

total swelling in this experiment, i.e. most of the deformation is permanent, fitting with previous polymer research (Busch and Gensterblum, 2011; Day et al., 2008; Wind et al., 2003).

3.2. Swelling of dolomite/coal/epoxy

We performed swelling experiments on Brzeszcze 364 coal samples to test the homogeneity of CO_2-induced swelling of this coal and how the local swelling is distributed in time and space. This will help constrain the representability of bulk swelling measurements such as those by Hol and Spiers (2012). The test assembly used here is a sample composed of dolomite (as a reference), epoxy (glue) and a mm-sized cube of Brzeszcze 364 coal (the example sample shown in Fig. 1; see also Fig. 6). In the studied area, the intermediate epoxy is about 300 μm wide. In reflected light, the bedding plane of the coal contains irregularly shaped structures, interpreted to be different macerals and minerals (Fig. 6a). This structure creates an initial topography of about 1 μm (Fig. 6b–c). At the end of experiment dolcoal1, the epoxy bulges out with a maximum height of 5–6 μm with respect to the dolomite and

the coal (Fig. 6b).

Exposure to CO_2 leads to swelling of the epoxy and the coal (Fig. 6, Supplementary Video V3 with the results of dolcoal3). The epoxy deformation is comparable to the results of dol2 and dol5. Depending on the experiment, the coal swells between 1.5 and 4.5 μm (always perpendicular to the bedding; see Fig. 7), and this swelling is fully reversible. Using the thickness of the inserted coal cube, this corresponds to 0.041–0.125% swelling strain. The total swelling depends on pressure and experiment duration, and swelling exhibits a power law time-dependence with exponents between 0.4 and 0.7, see Fig. 7. Studying the results of dolcoal3 in detail (Fig. 6), there is micrometer variability in how much coal swells. This correlates to the initial topography (as can be seen from comparison between Fig. 6c and e, and in Fig. 6f), and to the coal surface structure as visible in reflected light microscopy (Fig. 6a). This clearly demonstrates the local heterogeneous swelling properties of mm-sized coal samples, to our knowledge for the first time measured at sub-micrometer lateral resolution. The height distributions (Fig. 7b) show an initial shrinkage of the coal after CO_2 introduction, related to the thermo-elastic effects upon the pressure and temperature
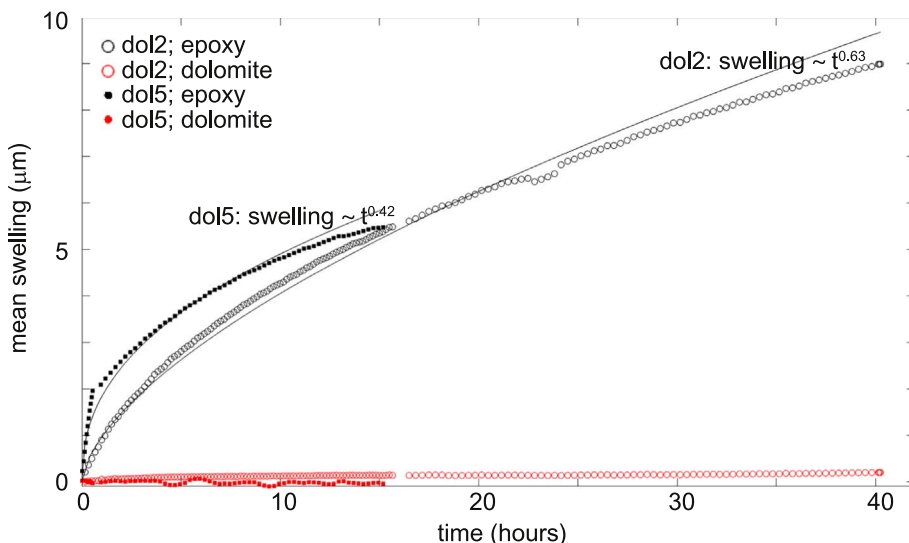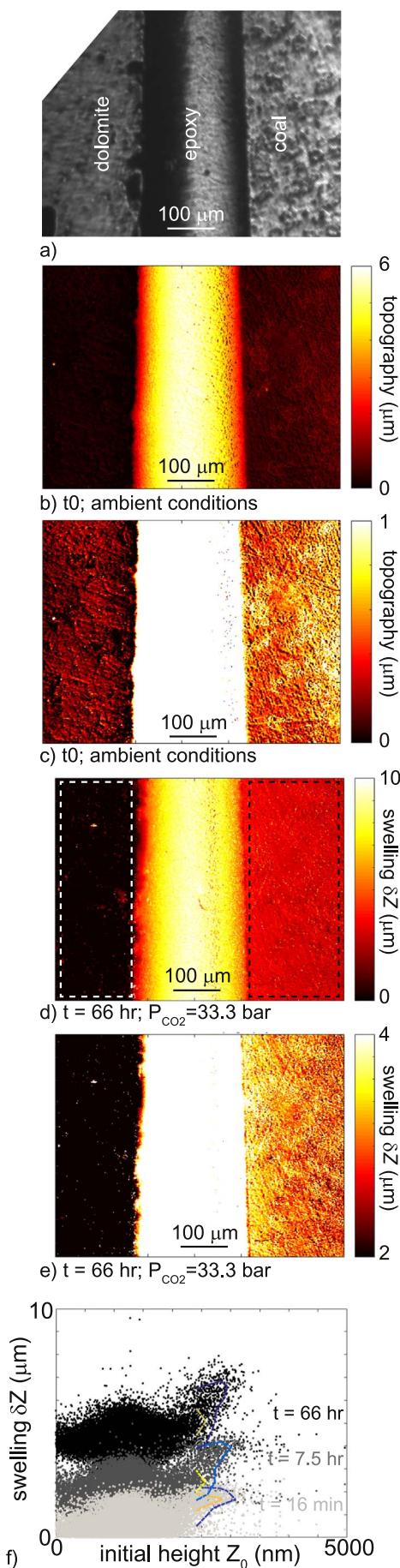

Fig. 5. Average swelling δz (μm) versus time for dol2 and dol5; epoxy in black and dolomite for reference in red. For dol5 there is a 3 bar pressure drop after the first hour (see Table 1), which changed the slope of the swelling curve. The power law fit of the epoxy swelling is shown in black, with the corresponding time exponents. (For interpretation of the references to color in this figure legend, the reader is referred to the web version of this article.)

a)

b) t0; ambient conditions

c) t0; ambient conditions

d) t = 66 hr; P$_{CO_2}$=33.3 bar

e) t = 66 hr; P$_{CO_2}$=33.3 bar

f)

Fig. 6. Coal swelling. See also Supplementary Video V3, which shows the swelling of epoxy and coal through time; i.e. the equivalent of Fig. 6d–e. All three experiments are performed on the same sample. a) reflected light image taken with an optical microscope. There is an irregular pattern in the coal sample of light and dark spots, interpreted to be related to the maceral and mineral content. The bright spots could be the inorganic material (ash content 5.2%). b);c) initial map of dolomite and epoxy for experiment dolcoal3, with different vertical scales to highlight the initial epoxy (b) and coal (c) topography. Coal topography is related to the morphology visible in a) (interpreted to be the maceral and mineral distribution); d);e) differential map of dolcoal3 showing δz (swelling), after ~66 h of exposure. Color scale for δz in e) is adapted to show the heterogeneous swelling of individual coal macerals. Squares on d) indicate areas from which averages are taken that are shown in Fig. 7. f) Initially high macerals exhibit slightly more swelling, shown by the change in angle of the 'tail' compared with the bulk of the data. Contourplots are added to guide the eye.

change. Taking the evolution of standard deviation of the height with time as a proxy for the coal roughness, there is a slow drop in the first 10 h (i.e. the surface becomes smoother), after which it recovers (inset in Fig. 7b).

3.3. Swelling in shales

We also used our set-up to measure CO_2-induced deformation in the Pomeranian shale and in the Green River shale (Table 1). In the interpretation of these multiple day exposure experiments it should be taken into account that we are looking at surface effects of 3-D samples, which are semi-confined as a result of the epoxy sample construction. Swelling is hence only possible in the vertical direction. Before the experiments we scanned these samples with SEM and EDS analysis was performed. For the experiments on Pomeranian shale and on Green River Shale we have, respectively, a high (Fig. 8a) and a low resolution (Fig. 9a) backscattered electron image of roughly the same area that is imaged with the white light interferometer. These images are taken with a Hitachi TM3000 (table-top) electron microscope with EDS capability, using a 15 kV acceleration voltage. This allowed identification of an area rich in organic matter, indicated with circles throughout Figs. 8 and 9. Even though the samples were polished, the final roughness still contained micron-sized differences between a few recognizable minerals, enabling correlation between the images obtained with secondary electrons (composition, Figs. 8a, 9a) and the white light interferometer (topography, Figs. 8b, 9b). Note that following the CO_2-sorption results on shales with different OM and clay content of Lutyński et al. (2017), we can expect more swelling of the organic matter than of the clay matrix.

To first focus on the Pomeranian shale, the total deformation is very small, and not significant in a simple histogram of the topography at different times (Fig. 8c). Therefore, to first identify if there are small-scale local areas with movement, the standard deviation over time for each pixel is plotted in Fig. 8d. There are some mineral shaped areas with high standard deviation, which means these either move up or down. Since each measurement is averaged over the entire sample surface (Fig. 2), if the majority of the surface swells, then those areas that swell less will appear as if they are moving down. Full sample-scale differential map-views of deformation are noisy, due to the fine-grained nature of shale versus the pixel size of 979 nm, i.e. one pixel usually covers multiple particles. Therefore, we focus on the area with organic matter only (which also exhibits a high standard deviation), see Fig. 8e–g. A close-up of this area (Fig. 8e) indicates that within this patch of organic matter + clay + pyrite there is one 20 × 20 μm area that exhibits more swelling than the surrounding surface. The average swelling of this area only (Fig. 8f) is compared with the average swelling of the area of Fig. 8e (excluding the data of Fig. 8f), and is shown in Fig. 8g. Within the first five hours this area swells 250–300 nm, i.e. just above the measurement resolution of a rough surface. After 5 h swelling stops and the height reaches a steady state value. Note also how the height of the surrounding area exhibits very little change. To clarify the trend, we fitted a moving median for which the time-window is
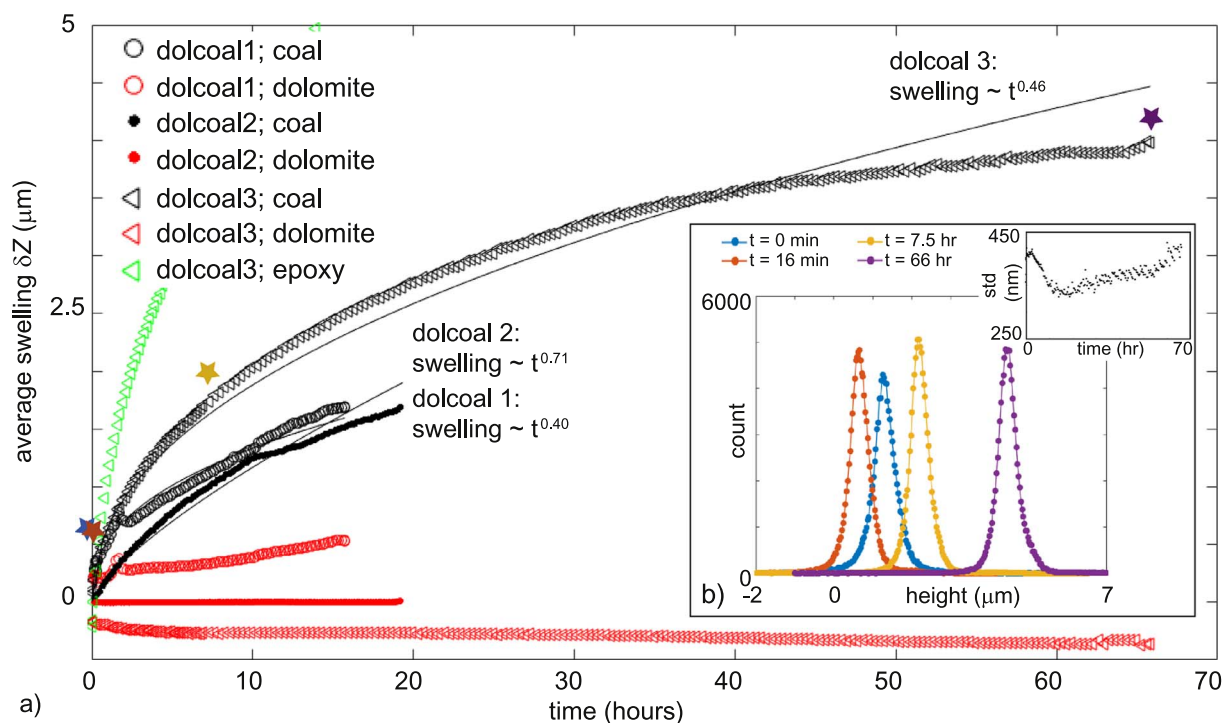
Fig. 7. Average swelling (μm) versus time (hours) for experiments dolcoal1, dolcoal2 and dolcoal3. These experiments were performed at different pressures, see Table 1. For dolcoal1 there was a 7 bar pressure drop after the first 2 h (see Table 1), which changed the slope of the swelling curve. The curve fit of the epoxy swelling is shown in black (time exponents are indicated in the plot). The stars indicate the timing of the datasets for which the histograms are shown in b); b) height distributions at different times. Note how the introduction of CO_2 causes an apparent initial shrinking of the coal. The inset shows how the standard deviation (std) of the height distributions decreases in the first 10 h which indicates an initial smoothening of the surface after CO_2 introduction. (For interpretation of the references to color in this figure legend, the reader is referred to the web version of this article.)

determined through logarithmic binning (Fig. 8g). Fitting a power-law only to the moving median over the first 4 h gives a time exponent of 0.37.

For the Green River shale, the organic matter visible in the electron image (Fig. 9a) is clearly visible in the topography as a slightly higher area (Fig. 9b). Given the visible organic matter at the surface (and thus easy CO_2 access), some swelling of this region would be expected. However, this area does not exhibit significant swelling (Fig. 9c). This could be related to the small lateral extent of this organic matter patch: it has a high aspect ratio and it is < 10 pixels (or 9.79 μm) wide. This limited lateral extent might be indicative of low thickness, and if the patch of organic matter is too thin there might not be sufficient sorption sites to lead to measurable sorption (> 200 nm). In contrast, an elongated patch on the right side of Fig. 9 does exhibit high standard deviations (indicated with the dotted box), even though there is no organic matter visible at the surface (Fig. 9a). The SEM images of these two shales show that pyrite and organic matter are often found in close proximity (as is also visible in Fig. 8a). This area contains some pyrite, i.e. this unidentified patch of high movement could be an expression of organic matter present just below the surface. The white light interferometer measures relative uplift of the surface only, which in effect is a sum of all processes occurring in the total sample volume as CO_2 diffuses into it. Typical interaction volumes of secondary electron microscopes are on the micrometer-scale, so if there is indeed organic matter below the surface, the swelling force is sufficient to lift a micrometer or more of the shale without fracturing it. A close-up of this area is shown in Fig. 9d–f. There is a small area of approximately 8 × 20 μm that exhibits significant swelling (Fig. 9e; note the 10 × increase in vertical scale compared to Fig. 9d). This area swells on average about 850 nm compared to its surroundings (Fig. 9f), though locally it reaches 3 μm (Fig. 9e). The total process takes about 10 h, after which the topography reaches a steady height. Fitting a powerlaw to the entire recorded dataset gives a time-exponent of 0.51, but the fit is poor ($R^2 = 0.61$).

4. Discussion

4.1. Advantages and limitations of the method

Using a novel experimental method we have measured swelling dynamics of a coal and two shale samples upon CO_2 exposure. By tracking the surface movement over time the use of the interferometer provides precise, quantitative data on local deformation and/or how local reactions lead to surface changes in solid materials. The method presented here can measure bulk swelling through averaging over the entire surface, as well as measure local swelling of individual components whilst exposed to a pressurized medium. It has sub-micron lateral and vertical resolution, and the exact same surface can be imaged with a range of microscopes before and after the experiments. Moreover, the current set-up allows the use of different types of swelling-inducing media, provided they are transparent (i.e. different solutions and gases). Finally, the demonstrated method can be applied to any type of composite or initially permeable reactive sample which can be made impermeable with epoxy, a cheap material. Overall, the presented procedure is an extremely versatile and low-cost method.

With the set-up presented here, the vertical resolution over time is 200 nm. The vertical resolution is independent of the combination of lenses, and is higher than the resolution of most micro-tomography methods (e.g. Karacan, 2007, 2003; Kobchenko et al., 2011; Pluymakers et al., 2017; Renard et al., 2016). With the lens combination used here, the lateral resolution was 979 nm, i.e. sufficient to identify and track individual minerals and macerals. An obvious generic limitation of microscopy measurements is the trade-off between pixel size and lateral extent of the measurement. The lateral extent of the measurement can be increased by using stitching, the feasibility of which depends on the availability and precision of an automated stage and the measurement speed of the interferometer versus desired sampling rate. In the datasets presented here we used only single (i.e. non-stitched) measurements. Assuming the surface can be imaged without a
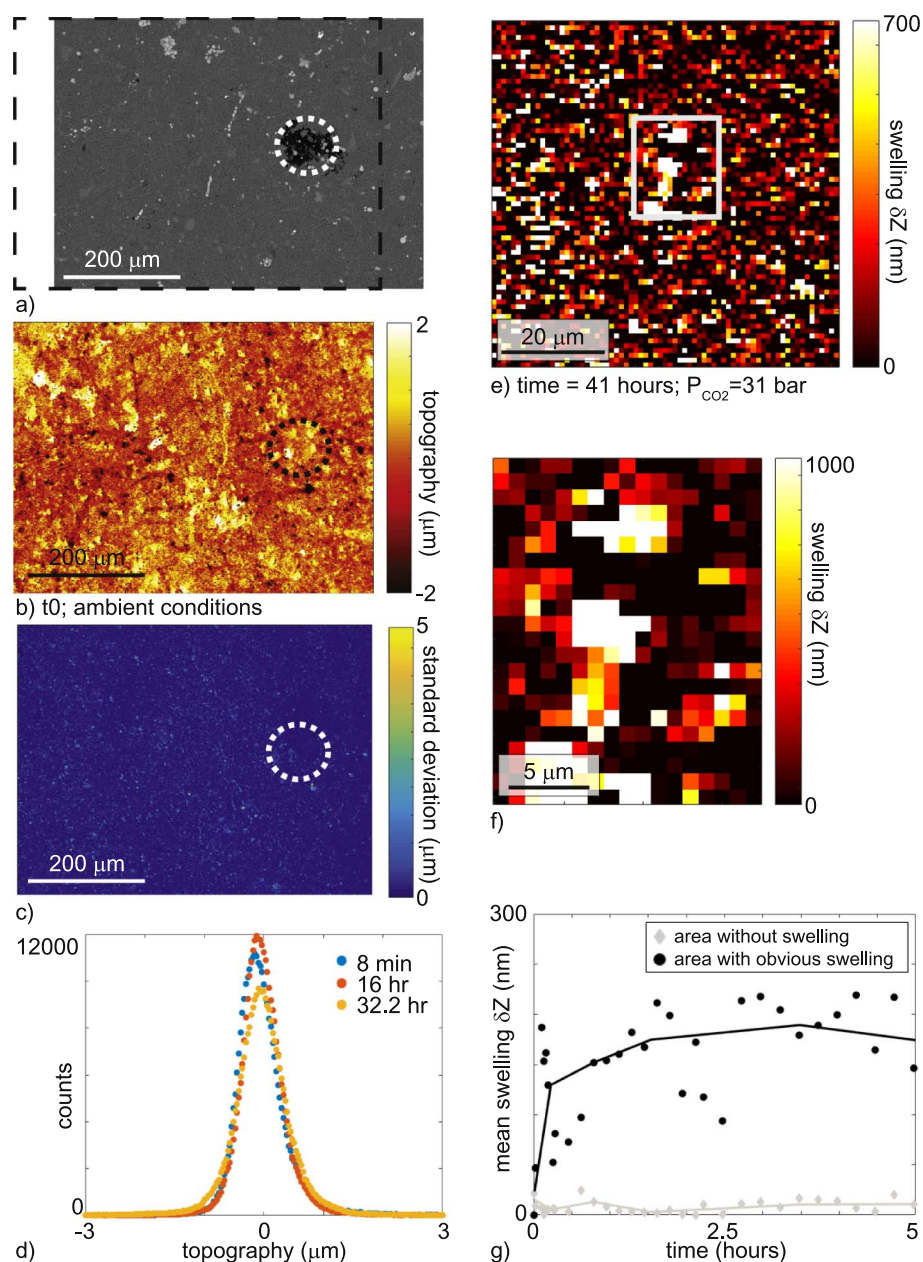
Fig. 8. Deformation of sample CO_2_11, Pomeranian shale. The circles indicates the location of a patch of organic matter (black), interspersed with pyrite (bright), an area which is investigated in greater detail in Fig. 8e–g); a) backscattered electron image taken before completing sample assembly. The dotted rectangle indicates the approximate location of topography measurements shown in b) where the initial topography is measured with the white light interferometer; c) map with the standard deviation of each pixel through time. High numbers indicate the pixel moved in height during the experiment. In approximately the same location as where the organic matter was present in the SEM image (white circle) there are measurable topography changes; d) histogram of the height data at different times. There is a small change in the histogram shape, close to the measurement error of 200 nm. 8e–g) Close-up of the area containing organic matter; e) a 20×20 µm region exhibits more swelling than the surrounding shale surface. This is shown in further close-up in f). Note the change in scale of the z-axis; g) mean swelling of the area without organic matter and the smaller area with organic matter versus time. The solid line is the same data set smoothed with a median filter with logarithmic binning of time. On average this patch swells about 250 nm in the first hours of the experiment.

coating, electron microscopy provides equal or higher lateral resolution (Wang et al., 2017), but it cannot provide high resolution data of any vertical deformation and has more limitations for the type and pressure of swelling-inducing medium to use. An easy improvement to the setup presented here would be the addition of carefully volume-calibrated pressure vessels, include an access to vacuum, and add a precise thermocouple. This would allow simultaneous measurements of bulk sorption and deformation, similar to Karacan (2007, 2003). Since epoxy itself is a reactive material (to CO_2 and acetone), for composite samples assembled using reactive epoxy interpretation might prove complicated. The supplementary materials contain further tips and tricks on how to best build and use this assembly.

4.2. Dynamics of coal swelling

We have tracked the bulk swelling behavior of coal, and showed heterogeneity in the swelling behavior of individual macerals. Similar local heterogeneous swelling behavior of coal was also reported by Karacan (2007, 2003) in microtomography experiments with a 250 µm

voxel resolution. Note that in their experiments it was not possible to correlate the behavior of the same location one-on-one with observation by other microscopy methods. Moreover, high resolution swelling measurements so far have been mainly measured as bulk-swelling on mm- to cm-sized samples in the laboratory (e.g. Hol and Spiers, 2012). These previous studies report the bulk swelling of a mm-sized Brzeszcze coal sample (i.e. the same coal as used here) exposed to CO_2 at 40 °C, using an eddy current sensor with a 50 nm resolution. Comparing their bulk swelling measurements at 3 MPa CO_2 pressure to ours, the average swelling strain experienced by our samples is smaller: ~0.4% by Hol and Spiers vs. 0.13% here, though our samples did not reach full equilibrium yet after 66 h of CO_2 exposure. First, there is a ~20 °C temperature difference. A decrease in temperature would lead to a small increase in swelling, i.e. opposite to what is observed. Second, in our experiments, there is only one exposed face during the experiments. This increases the diffusion path length of CO_2 in the sample. Combined with the passive confinement provided by the epoxy, this will lead to non-equilibrium swelling. Similar non-equilibrium swelling of Brzeszcze coal upon exposure to CH_4 has also been reported by Liu et al.
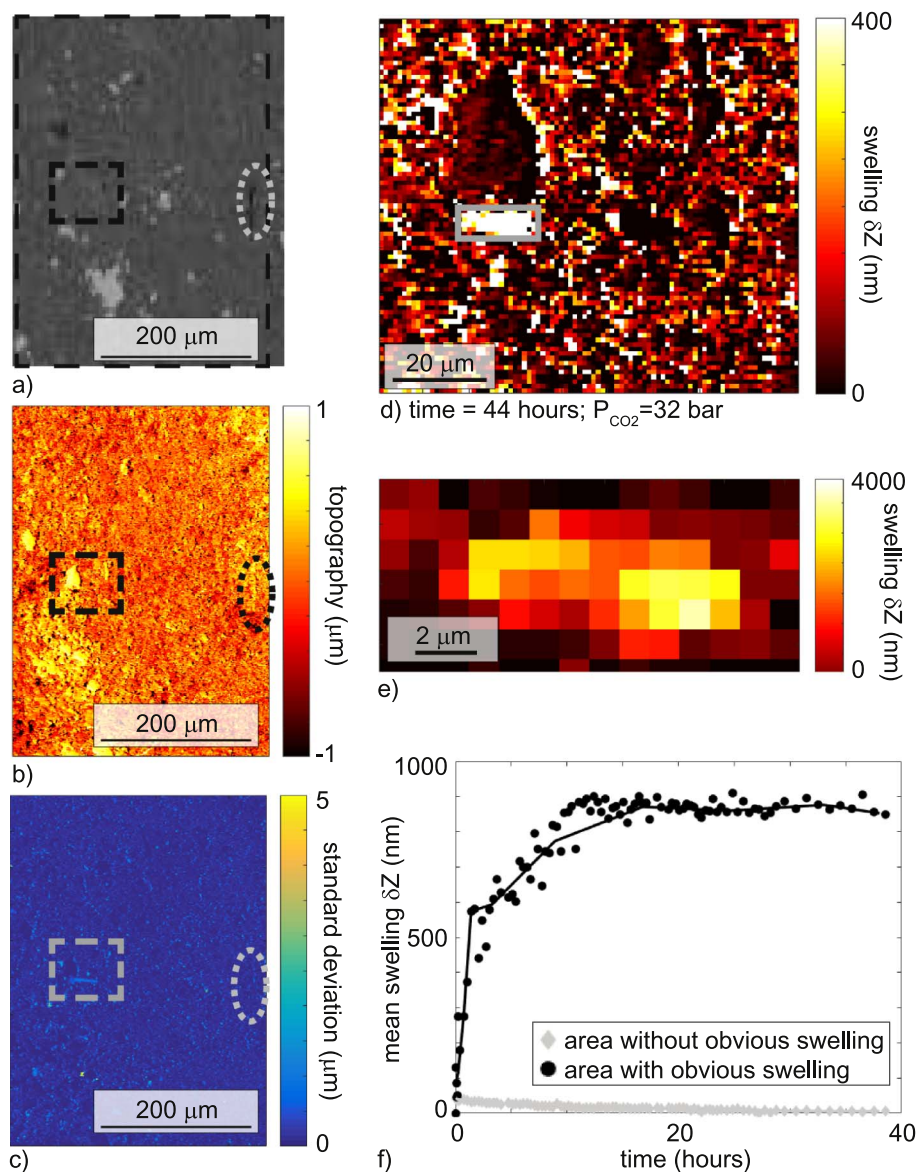
Fig. 9. Deformation of CO_2_12, GRS shale. The dotted circle indicates the elongated patch of organic matter (black) in all images; the squares indicate the area analyzed in Fig. 9d–f; a) backscatter electron image. Bright colors correspond to pyrite grains, and the location imaged with white light interferometry is indicated with the outer black box; b) the initial surface topography as measured with white light interferometry; c) the standard deviation of δZ over time for each pixel. High values indicate the pixel moved over time. There is very little movement in the patch that contains organic matter. There is significant movement of the area analyzed in more detail in Fig. 9d–f; d) a roughly $8 \times 20\,\mu m$ area exhibits more swelling than the surrounding shale surface, despite no obvious organic matter at the surface analyzed with SEM (Fig. 9a). This swelling is shown in further close-up in e) - note the change in scale of the z-axis; f) mean swelling of the area without obvious swelling and the smaller area with obvious swelling versus time. The solid line is the same data set smoothed with a median filter with logarithmic binning of time. On average, this small patch swells about 850 nm in the first 20 h.

(2016). Third, the sample was kept at ambient conditions in between experiments, and any residual water in coal samples (even atmospheric water) strongly reduces sorption of CO_2 and the associated swelling (Busch and Gensterblum, 2011; Day et al., 2008). Even though the current results do not allow for exact determination of the kinetics of swelling, all determined bulk rates all were close to a power law time dependence with an exponent of ~0.5, which, assuming pure Fickian diffusion, would be indicative of a swelling process controlled by the diffusion rate of CO_2 into the matrix. This is in line with studies that show coal sorption and swelling rates to be dependent on sample size, and which accordingly assume diffusion-controlled transport (Busch and Gensterblum, 2011; Gruszkiewicz et al., 2009; Liu et al., 2016; Lutynski and González González, 2016; Staib et al., 2014). The swelling curves presented here are the result of the diffusion of molecules into the sorbent (i.e. the coal), and can be related to diffusive transport models that consider the effects of reversible adsorption processes on the distribution of diffusing models, such as Dumazer et al. (2017). Dumazer et al. include an explicit formula for the adsorption flux at a boundary, where the integrated flux would provide the number of molecules adsorbed by the boundary, which should follow the same time-dependence as the swelling surface we measured.

The 0.13% swelling strain experienced on average by our samples corresponds to an average swelling of ~4 μm, where micrometer-sized patches exhibit up to 1 μm differences. Local swelling is thus up to ~25% different compared to the average value. This laterally variable swelling followed the geometrical pattern seen in the optical microscopy image (Fig. 6a) and the topography (Fig. 6b; c), which is interpreted to correspond to the composition of the surface, i.e. the macerals and the minerals. Moreover, initially high areas swelled more (Fig. 6f). Such heterogeneous swelling supposedly will generate tensile stresses in the coal matrix, and could lead to microcracking (as also postulated by Hol et al., 2012; Liu et al., 2017). This type of microcracks will provide fast transport paths, and should thus accelerate the bulk swelling rate of coal (cf. Hol et al., 2012).

4.3. Dynamics of heterogeneous deformation in shale

We have measured differential swelling for two different shale types, the Pomeranian and the Green River shales. This type of high resolution differential shale swelling experiments shows some similarity to the experiments performed by Wang et al. (2017). They investigated lateral swelling in clay rocks as a result of exposure to varying air humidity using electron microscopy. Qualitatively, they found similar results as we do: swelling is composition-dependent. In

their experiments, water-induced swelling occurs mostly in the clay-rich areas, and not so much in the (larger) carbonate, quartz and pyrite grains. There are two main differences between these experiments. First, we investigated CO_2-induced swelling in room humidity samples, not humidity-induced swelling in perfectly dry samples. Even though CO_2-induced clay swelling is expected (Busch et al., 2016; Lutyński et al., 2017), since our method is geared towards measuring differential swelling and not bulk values, this is difficult to capture in these experiments. We choose full shale windows (i.e. without reference surface and epoxy) because of the choice to focus on the differential swelling behavior of organic matter versus that of the clay particles. Second, in the experiments of Wang et al. (2017), lateral movements were captured instead of vertical movement, since their samples were unconfined. The epoxy provides a passive confinement, meaning that the swelling is driven by the diffusion of CO_2 into the matrix so motion here is perpendicular to the surface. That means that if any sorption-induced swelling leads to vertical surface deformation, our experimental setup can capture it.

The preferential CO_2-sorption and associated swelling of patches of organic matter has been hypothesized before, where the process of methane desorption and subsequent CO_2 sorption could lead to enhanced shale gas recovery (cf. Middleton et al., 2015). To our knowledge, these are the first results that capture the dynamics of the swelling process of micrometer-sized patches of organic matter compared to the matrix, for as little swelling as 250 nm. Note that with the current data it is not possible to estimate and compare the swelling strain of the organic matter patches, since their thickness is unknown. We also capture measurable surface deformation (a maximum average of 850 nm) of what supposedly is the expression of organic matter swelling just below the surface. This type of data shows similarity to analogue surface deformation experiments for intrusions, where rate and shape of surface deformation are related to the shape of the intrusion (such as Guldstrand et al., 2017). Combining these methods would enable the determination of the approximate 3D shape of the organic matter.

For both shale experiments, there was no clear time dependence for the swelling of the organic matter. The total local swelling possible in shales is finite; in the Pomeranian shale maximum swelling was reached within ~4 h, and in the Green River shale in ~20 h. This is easily explained by the finite thickness of the scattered patches of organic matter, from which logically follows there is thus a finite number of sorption sites within each patch of organic matter. Now, assuming a scenario in which CO_2 is used as fracking fluid in shales (as also suggested by Middleton et al., 2015), our results suggest CO_2 adsorption to organic patches can create local, micrometer-sized asperities within the first few hours after opening the fracture. Since these asperities are spatially related to the patches of organic matter, the number and location will be related to the location of organic matter concentrations within the matrix. Moreover, since these patches are limited in extent, the total swelling will be determined to the thickness or size of each patch of organic matter, given that swelling is finite, as also shown in the experiments (Figs. 8 and 9). These local asperities might have effects on crack propagation and therefore on the fluid dynamics in the narrow crack tip within the first hours to days after CO_2 exposure. However, in our experiments we showed < 1 μm sized asperities. Sorption-induced swelling of organic matter can be expected to be dependent on the pressure and temperature conditions of CO_2 (similar to coal). However, since typical proppant sizes are up to 500 μm this process should be of minor importance in propped fractures.

5. Conclusions

We have built a working micro-pressure chamber that can hold pressures up to 100 bar, and we used a white light interferometer to directly measure CO_2-induced changes to surface topography for unreactive dolomite, and reactive coals and shale samples. This novel experimental approach allows measuring the dynamics of both bulk and local deformation of the sample while exposing it to fluids at high pressure. The advantages of this set-up lie in the unprecedented sub-micrometer spatial and vertical resolution, and the versatility with respect to sample and pressurizing medium.

We used the presented method successfully to monitor the swelling over time of epoxy/dolomite, coal/epoxy/dolomite and shale samples. Our conclusions are the following:

- Epoxy swelling is shown to be homogeneous and mostly permanent. It exhibits a standard power law Fickian time-dependence with a time exponent of ~0.5.
- Swelling of a Brzeszcze coal sample is heterogeneous. Initially higher components exhibit up to 25% more swelling than the average, bulk swelling values. Bulk swelling also exhibits an approximate time-dependence of ~0.5.
- Measurements targeted at observing local swelling in shales indicate swelling of small, micrometer-sized, patches of organic matter. An average 250 nm swelling in 4 h is recorded for a 20 × 20 μm patch of organic matter in the Pomeranian shale. For a Green River shale sample, for a 8 × 20 μm location, we record an average 850 nm swelling (though locally this can be 3 to 4 μm) for what is interpreted to be organic matter just below the surface.

Supplementary data to this article can be found online at https://doi.org/10.1016/j.coal.2018.01.007.

References

Bachaud, P., Berne, P., Renard, F., Sardin, M., Leclerc, J.P., 2011. Use of tracers to characterize the effects of a CO_2-saturated brine on the petrophysical properties of a low permeability carbonate caprock. Chem. Eng. Res. Des. 89, 1817–1826. http://dx.doi.org/10.1016/j.cherd.2010.11.004.

Brochard, L., Vandamme, M., Pellenq, R.J.-M., Fen-Chong, T., 2012. Adsorption-induced deformation of microporous materials: coal swelling induced by CO_2–CH_4 competitive adsorption. Langmuir 28, 2659–2670. http://dx.doi.org/10.1021/la204072d.

Busch, A., Gensterblum, Y., 2011. CBM and CO_2-ECBM related sorption processes in coal: a review. Int. J. Coal Geol. 87, 49–71. http://dx.doi.org/10.1016/j.coal.2011.04.011.

Busch, A., Alles, S., Gensterblum, Y., Prinz, D., Dewhurst, D.N., Raven, M.D., Stanjek, H., Krooss, B.M., 2008. Carbon dioxide storage potential of shales. Int. J. Greenh. Gas Control 2, 297–308. http://dx.doi.org/10.1016/j.ijggc.2008.03.003.

Busch, A., Bertier, P., Gensterblum, Y., Rother, G., Spiers, C.J., Zhang, M., Wentinck, H.M., 2016. On sorption and swelling of CO_2 in clays. Geomech. Geophys. Geo Energy Geo Resour. 2, 111–130. http://dx.doi.org/10.1007/s40948-016-0024-4.

Day, S., Fry, R., Sakurovs, R., 2008. Swelling of Australian coals in supercritical CO_2. Int. J. Coal Geol. 74, 41–52. http://dx.doi.org/10.1016/j.coal.2007.09.006.

de Jong, S.M., Spiers, C.J., Busch, A., 2014. Development of swelling strain in smectite clays through exposure to carbon dioxide. Int. J. Greenh. Gas Control 24, 149–161. http://dx.doi.org/10.1016/j.ijggc.2014.03.010.

Dumazer, G., Flekkøy, E., Renard, F., Angheluta, L., 2017. Transient anomalous diffusion regimes in reversible adsorbing systems. Phys. Rev. E 96, 42106. http://dx.doi.org/10.1103/PhysRevE.96.042106.

Edlmann, K., Haszeldine, S., McDermott, C.I., 2013. Experimental investigation into the sealing capability of naturally fractured shale caprocks to supercritical carbon dioxide flow. Environ. Earth Sci. 70, 3393–3409. http://dx.doi.org/10.1007/s12665-013-2407-y.

Elkhoury, J.E., Ameli, P., Detwiler, R.L., 2013. Dissolution and deformation in fractured carbonates caused by flow of CO_2-rich brine under reservoir conditions. Int. J. Greenh. Gas Control 16, S203–S215. http://dx.doi.org/10.1016/j.ijggc.2013.02.023.

Ellis, B.R., Bromhal, G.S., McIntyre, D.L., Peters, C.A., 2011. Changes in caprock integrity

due to vertical migration of CO_2 -enriched brine. Energy Procedia 4, 5327–5334. http://dx.doi.org/10.1016/j.egypro.2011.02.514.

Fondriest, M., Aretusini, S., Di Toro, G., Smith, S.A.F., 2015. Fracturing and rock pulverization along an exhumed seismogenic fault zone in dolostones: the Foiana Fault Zone (Southern Alps, Italy). Tectonophysics 654, 56–74. http://dx.doi.org/10.1016/j.tecto.2015.04.015.

Giesting, P., Guggenheim, S., Koster van Groos, A.F., Busch, A., 2012. Interaction of carbon dioxide with Na-exchanged montmorillonite at pressures to 640 bars: implications for CO_2 sequestration. Int. J. Greenh. Gas Control 8, 73–81. http://dx.doi.org/10.1016/j.ijggc.2012.01.011.

Gruszkiewicz, M.S., Naney, M.T., Blencoe, J.G., Cole, D.R., Pashin, J.C., Carroll, R.E., 2009. Adsorption kinetics of CO_2, CH_4, and their equimolar mixture on coal from the Black Warrior Basin, West-Central Alabama. Int. J. Coal Geol. 77, 23–33. http://dx.doi.org/10.1016/J.COAL.2008.09.005.

Guldstrand, F., Burchardt, S., Hallot, E., Galland, O., 2017. Dynamics of surface deformation induced by dikes and cone sheets in a cohesive coulomb brittle crust. J. Geophys. Res. Solid Earth 122, 8511–8524. http://dx.doi.org/10.1002/2017JB014346.

Hol, S., Spiers, C.J., 2012. Competition between adsorption-induced swelling and elastic compression of coal at CO_2 pressures up to 100MPa. J. Mech. Phys. Solids 60, 1862–1882. http://dx.doi.org/10.1016/j.jmps.2012.06.012.

Hol, S., Peach, C.J., Spiers, C.J., 2011. Applied stress reduces the CO_2 sorption capacity of coal. Int. J. Coal Geol. 85, 128–142. http://dx.doi.org/10.1016/J.COAL.2010.10.010.

Hol, S., Spiers, C.J., Peach, C.J., 2012. Microfracturing of coal due to interaction with CO_2 under unconfined conditions. Fuel 97, 569–584. http://dx.doi.org/10.1016/J.FUEL.2012.02.030.

Karacan, C., 2003. Heterogeneous Sorption and Swelling in a Confined and Stressed Coal During CO_2 Injection. http://dx.doi.org/10.1021/EF0301349.

Karacan, C., 2007. Swelling-induced volumetric strains internal to a stressed coal associated with CO_2 sorption. Int. J. Coal Geol. 72, 209–220. http://dx.doi.org/10.1016/j.coal.2007.01.003.

Kobchenko, M., Panahi, H., Renard, F., Dysthe, D.K., Malthe-Sørenssen, A., Mazzini, A., Scheibert, J., Jamtveit, B., Meakin, P., 2011. 4D imaging of fracturing in organic-rich shales during heating. J. Geophys. Res. 116, B12201. http://dx.doi.org/10.1029/2011JB008565.

Lin, J., Ren, T., Wang, G., Booth, P., Nemcik, J., 2017. Experimental study of the adsorption-induced coal matrix swelling and its impact on ECBM. J. Earth Sci. 28, 917–925. http://dx.doi.org/10.1007/s12583-017-0778-9.

Liu, F., Lu, P., Griffith, C., Hedges, S.W., Soong, Y., Hellevang, H., Zhu, C., 2012. CO_2–brine–caprock interaction: reactivity experiments on Eau Claire shale and a review of relevant literature. Int. J. Greenh. Gas Control 7, 153–167. http://dx.doi.org/10.1016/j.ijggc.2012.01.012.

Liu, J., Peach, C.J., Zhou, H., Spiers, C.J., 2015. Thermodynamic models for swelling of unconfined coal due to adsorption of mixed gases. Fuel 157, 151–161. http://dx.doi.org/10.1016/j.fuel.2015.04.070.

Liu, J., Peach, C.J., Spiers, C.J., 2016. Anisotropic swelling behaviour of coal matrix cubes exposed to water vapour: effects of relative humidity and sample size. Int. J. Coal Geol. 167, 119–135. http://dx.doi.org/10.1016/J.COAL.2016.09.011.

Liu, J., Fokker, P.A., Spiers, C.J., 2017. Coupling of swelling, internal stress evolution, and diffusion in coal matrix material during exposure to methane. J. Geophys. Res. Solid Earth 122, 844–865. http://dx.doi.org/10.1002/2016JB013322.

Lutynski, M., González González, M., 2016. Characteristics of carbon dioxide sorption in coal and gas shale – the effect of particle size. J. Nat. Gas Sci. Eng. 28, 558–565. http://dx.doi.org/10.1016/j.jngse.2015.12.037.

Lutyński, M., Waszczuk, P., Słomski, P., Szczepański, J., 2017. CO_2 sorption of

Pomeranian gas bearing shales – the effect of clay minerals. Energy Procedia 125, 457–466. http://dx.doi.org/10.1016/j.egypro.2017.08.153.

Michels, A., Hamers, J., 1937. The effect of pressure on the refractive index of CO_2: the Lorentz-Lorenz formula. Physica 4, 995–1006. http://dx.doi.org/10.1016/S0031-8914(37)80197-4.

Middleton, R.S., Carey, J.W., Currier, R.P., Hyman, J.D., Kang, Q., Karra, S., Jiménez-Martínez, J., Porter, M.L., Viswanathan, H.S., 2015. Shale gas and non-aqueous fracturing fluids: opportunities and challenges for supercritical CO_2. Appl. Energy 147, 500–509. http://dx.doi.org/10.1016/j.apenergy.2015.03.023.

Moore, T.A., 2012. Coalbed methane: a review. Int. J. Coal Geol. 101, 36–81. http://dx.doi.org/10.1016/j.coal.2012.05.011.

Neuville, A., Renaud, L., Luu, T.T., Minde, M.W., Jettestuen, E., Vinningland, J.L., Hiorth, A., Dysthe, D.K., 2016. Xurography for microfluidics on a reactive solid. Lab Chip. http://dx.doi.org/10.1039/C6LC01253A.

Nguyen, P., Fadaei, H., Sinton, D., 2013. Microfluidics underground: a micro-core method for pore scale analysis of supercritical CO_2 reactive transport in saline aquifers. J. Fluids Eng. 135, 21203. http://dx.doi.org/10.1115/1.4023644.

Olabode, A., Radonjic, M., 2014. Diagenetic influence on fracture conductivity in tight shale and CO_2 sequestration. Energy Procedia 63, 5021–5031. http://dx.doi.org/10.1016/j.egypro.2014.11.532.

Ougier-Simonin, A., Renard, F., Boehm, C., Vidal-Gilbert, S., 2016. Microfracturing and microporosity in shales. Earth-Sci. Rev. 162, 198–226. http://dx.doi.org/10.1016/j.earscirev.2016.09.006.

Perrier, L., Plantier, F., Gregoire, D., 2017. A novel experimental setup for simultaneous adsorption and induced deformation measurements in microporous materials. Rev. Sci. Instrum. 88, 35104. http://dx.doi.org/10.1063/1.4977595.

Pluymakers, A., Kobchenko, M., Renard, F., 2017. How microfracture roughness can be used to distinguish between exhumed cracks and in-situ flow paths in shales. J. Struct. Geol. 94, 87–97. http://dx.doi.org/10.1016/j.jsg.2016.11.005.

Porter, M.L., Jiménez-Martínez, J., Martinez, R., McCulloch, Q., Carey, J.W., Viswanathan, H.S., 2015. Geo-material microfluidics at reservoir conditions for subsurface energy resource applications. Lab Chip 15, 4044–4053. http://dx.doi.org/10.1039/c5lc00704f.

Radlinski, A., Mastalerzb, M., Hinde, A., Hainbuchner, M., Rauch, H., Baron, M., Lin, J., Fan, L., Thiyagarajan, P., 2004. Application of SAXS and SANS in evaluation of porosity, pore size distribution and surface area of coal. Int. J. Coal Geol. 59, 245–271. http://dx.doi.org/10.1016/j.coal.2004.03.002.

Renard, F., Cordonnier, B., Dysthe, D.K., Boller, E., Tafforeau, P., Rack, A., 2016. A deformation rig for synchrotron microtomography studies of geomaterials under conditions down to 10 km depth in the earth. J. Synchrotron Radiat. 23, 1030–1034. http://dx.doi.org/10.1107/S1600577516008730.

Rohmer, J., Pluymakers, A., Renard, F., 2016. Mechano-chemical interactions in sedimentary rocks in the context of CO_2 storage: weak acid, weak effects? Earth Sci. Rev. 157, 86–110. http://dx.doi.org/10.1016/J.EARSCIREV.2016.03.009.

Staib, G., Sakurovs, R., Gray, E.M., 2014. Kinetics of coal swelling in gases: influence of gas pressure, gas type and coal type. Int. J. Coal Geol. 132, 117–122. http://dx.doi.org/10.1016/j.coal.2014.08.005.

van Bergen, F., Spiers, C., Floor, G., Bots, P., 2009. Strain development in unconfined coals exposed to CO_2, CH_4 and Ar: effect of moisture. Int. J. Coal Geol. 77, 43–53. http://dx.doi.org/10.1016/j.coal.2008.10.003.

Wang, L.L., Yang, R.W., Chanchole, S., Zhang, G.Q., 2017. The time-dependent swelling of argillaceous rock under resaturated conditions. Appl. Clay Sci. 146, 186–194. http://dx.doi.org/10.1016/j.clay.2017.05.041.

Wind, J.D., Sirard, S.M., Paul, D.R., Green, P.F., Johnston, K.P., Koros, W.J., 2003. Relaxation dynamics of CO_2 diffusion, sorption, and polymer swelling for plasticized polyimide membranes. Macromolecules 36. http://dx.doi.org/10.1021/MA034359U.